

# Implications of the Super-K atmospheric data for the mixing angles $\theta_{13}$ and $\theta_{23}$

J. E. Roa<sup>1</sup>, D. C. Latimer<sup>2</sup>, and D. J. ErnsJt<sup>1</sup>

<sup>1</sup>*Department of Physics and Astronomy, Vanderbilt University, Nashville, Tennessee 37235 and*

<sup>2</sup>*Department of Physics and Astronomy, University of Kentucky, Lexington, Kentucky 40506*

(Dated: October 27, 2018)

A three-neutrino analysis of oscillation data is performed using the recent, more finely binned Super-K oscillation data, together with the CHOOZ, K2K, and MINOS data. The solar parameters,  $\Delta_{21}$  and  $\theta_{12}$ , are fixed from a recent analysis, and  $\Delta_{32}$ ,  $\theta_{13}$ , and  $\theta_{23}$  are varied. We utilize the full three-neutrino oscillation probability and an exact treatment of the Earth's MSW effect with a castle-wall density. By including terms linear in  $\theta_{13}$  and  $\varepsilon := \theta_{23} - \pi/4$ , we find asymmetric errors for these parameters  $\theta_{13} = -0.07^{+0.18}_{-0.11}$  and  $\varepsilon = 0.03^{+0.09}_{-0.15}$ . For  $\theta_{13}$ , we see that the lower bound is primarily set by the CHOOZ experiment while the upper bound is determined by the low energy  $e$ -like events in the Super-K atmospheric data. We find that the parameters  $\theta_{13}$  and  $\varepsilon$  are correlated — the preferred negative value of  $\theta_{13}$  permits the preferred value of  $\theta_{23}$  to be in the second octant, and the true value of  $\theta_{13}$  affects the allowed region for  $\theta_{23}$ .

PACS numbers: 14.60.Pq

Keywords: neutrino oscillations, three neutrinos, mixing angles, mass-squared differences

## I. INTRODUCTION

The experimental observation of neutrino oscillations implies that at least two of three neutrinos have mass, and the mass eigenstates differ from the flavor eigenstates. The vast majority of oscillation experiments [1, 2, 3, 4, 5, 6, 7, 8, 9, 10, 11, 12, 13, 14, 15, 16, 17, 18, 19, 20], including the null result from the CHOOZ reactor experiment [21], can be globally understood in terms of three mixing angles  $\theta_{jk}$ , with  $j = 1, 2, 3$  and  $j < k$ , one phase  $\delta$ , and two independent mass-squared differences  $\Delta_{kj} := m_k^2 - m_j^2$ . The separation between two of the mass-squared differences is sufficiently large so that the data from a given experiment, which may span some range of baselines and neutrino energies, can be approximately understood within the context of an effective two-flavor theory. Experiments detecting solar neutrinos [1, 2, 3, 4, 5, 6, 7, 8, 9, 10] and the long baseline (LBL) reactor experiment KamLAND [11, 12] are particularly sensitive to the mixing angle  $\theta_{12}$  and the mass-squared difference  $\Delta_{21}$  assuming the standard representation of the neutrino mixing matrix [22]. A three neutrino analysis [23] gives a value for the mixing angle  $\sin^2 \theta_{12} = 0.304^{+0.046}_{-0.034}$  ( $2 \sigma$  error), with a precision of 8% at  $3\sigma$ . The solar mass-squared difference is determined predominantly by the SNO data [10] and is found to be  $\Delta_{21} = 7.65^{+0.47}_{-0.40} \times 10^{-5} \text{ eV}^2$ . Atmospheric and accelerator beam stop neutrinos provide experimentalists with a good source with which to measure  $\theta_{23}$  and  $\Delta_{32}$ . MINOS [17, 18] predominantly determines  $\Delta_{32}$  while the mixing angle  $\theta_{23}$  is determined mainly by the Super-K atmospheric data [13, 14, 15, 16]. Present values for these parameters [23] are  $\Delta_{32} = 2.40^{+0.24}_{-0.22} \times 10^{-3} \text{ eV}^2$  and  $\sin^2 \theta_{23} = 0.50^{+0.13}_{-0.11}$ . The remaining mixing angle,  $\theta_{13}$ , mixes the two scales. This same analysis gives  $\sin^2 \theta_{13} \leq 0.040$ ; recent analyses hint at a value of  $\theta_{13}$  differing from zero [24, 25, 26]. Recent review articles can be found at Refs. [27, 28].

As we enter the era of precision measurements, global analyzes of neutrino data must employ a full three-neutrino framework in order to correctly assess the neutrino mixing parameters. This will become evident herein as we consider various experiments' impact upon the small parameters  $\theta_{13}$  and  $\varepsilon := \theta_{23} - \pi/4$ , the deviation of  $\theta_{23}$  from maximal mixing. The quantitative knowledge of  $\theta_{13}$  is a particularly important part of neutrino oscillation phenomenology because it sets the magnitude of possible CP violating effects as well as the size of effects that might be used to determine the neutrino mass hierarchy. There are presently three new reactor experiments planned or under construction which are designed to measure  $\theta_{13}$ , Daya Bay [29], Double CHOOZ [30], and RENO [31]; an LBL experiment is also planned, T2K [32]. The subsequent generation of experiments, which will be designed to ascertain the level of CP violation, cannot proceed until the current generation better determines the value of  $\theta_{13}$ . In addition, a more quantitative knowledge of the mixing angles, and particularly of  $\theta_{13}$ , can help discern between models and symmetries of the physics that underlies neutrino mixing [33]. The deviation of  $\theta_{23}$  from maximal mixing is also important in model building as it might indicate the presence of a broken symmetry. At short baselines, the oscillation probabilities which might probe the mixing angle  $\theta_{13}$  are quadratic in this small parameter; however, we have previously shown there are terms in the oscillation probability which are linear and appreciable at very long baselines (VLBL) [34, 35, 36] and arise from interference between the oscillations driven by the two mass-squared differences. This is also a region of the parameter space where one can look [37, 38] for CP violating effects. The sub-GeV data set of the Super-K atmospheric experiments is potentially sensitive to such effects. Furthermore, it was shown in Ref. [36] that there is a non-trivial relation between  $\varepsilon$  and  $\theta_{13}$  for sub-GeV neutrinos at VLBLs. As such, the extraction of these parameters from the at-

mospheric data requires a full three neutrino treatment since approximations overly simplify the correlations of the parameters.

We here investigate atmospheric neutrino oscillations with the full three neutrino oscillation probabilities. Because we do not use truncated expansions, all terms linear in  $\theta_{13}$  and  $\varepsilon$  will be considered as well as higher order contributions. We do not expect a large change in the extracted parameters as only a limited number of the Super-K data bins lie in the region where linear terms will be significant. On the other hand, in the context of atmospheric data,  $\theta_{13}$  is itself a small effect as is the octant of  $\theta_{23}$ . Small effects can sometimes have a proportionally larger impact on something that is inherently small. In keeping with the use of the full three neutrino oscillation probabilities, we also utilize the method proposed in Refs. [39, 40] to treat the MSW effect [41, 42]. With a castle wall density profile of the earth, this treatment of the MSW effect is exact so that approximate expressions for the oscillation probabilities are not needed. We also include a model for the multi-ring events, a data subset often neglected.

## II. ANALYSIS

In vacuo, the probability that a neutrino of flavor  $\alpha$  and energy  $E_\nu$  will be detected as a neutrino of flavor  $\beta$  after traveling a distance  $L$  is given by

$$\mathcal{P}_{\alpha\beta}(L/E_\nu) = \delta_{\alpha\beta} - 4 \sum_{\substack{k < j, \\ j, k=1}}^3 (U_{\alpha j} U_{\alpha k} U_{\beta k} U_{\beta j}) \sin^2 \varphi_{jk}, \quad (1)$$

with  $\varphi_{jk} := 1.27 \Delta_{jk} L/E_\nu$ , where  $L$  is measured in kilometers,  $E_\nu$  in GeV, and the mass eigenvalues  $m_i$  in eV. The matrix  $U_{\alpha i}$  is the unitary matrix that relates the mass basis  $i$  to the flavor basis  $\alpha$ . We assume CP conservation so that the  $U_{\alpha i}$  are real. Neutrinos which propagate long distances through matter of sufficient densities can incur significant interactions which are diagonal in flavor. For matter of constant density, the upshot of these interactions is a modification of the effective mixing angles and mass-squared differences so that an oscillation formula similar to Eq. (1) holds. The density of the earth may be approximated as piecewise constant [43]. In addition, for certain energies and densities, the neutrinos can undergo parametric resonances in regions of varying densities [44]. To account for these interactions, we employ a simple model of the earth: a mantle of density 4.5 gm/cm<sup>3</sup> and a core of density 11.5 gm/cm<sup>3</sup> with radius 3486 km. Using the methods in Refs. [39, 40], we are able to fully incorporate an exact three neutrino model of the neutrino-matter interactions which automatically incorporates any possible parametric resonances.

Our interest is to study and extract the following parameters from the experimental data:  $\theta_{13}$ ,  $\theta_{23}$ , and  $\Delta_{32}$ . As such, we fix the solar mixing parameters from a re-

cent analysis [27],  $\theta_{12} = 0.58$  and  $\Delta_{21} = 8.0 \times 10^{-5}$  eV<sup>2</sup>. Given that there is no evidence to indicate CP violation, we assume CP conservation and take  $\delta = 0$ . We include the details of our analyses of the relevant experiments in the Appendix. We comment on them briefly here. The Super-K atmospheric data is statistically the most significant data set, and it covers a range of over four orders of magnitude in  $L/E$ . Our analysis employs the most recent more finely binned data [16], a necessity for studying the small parameters  $\theta_{13}$  and  $\varepsilon$ . We also include the most recent MINOS results [18], the K2K results [20], and the CHOOZ results [21].

In order to ascertain the importance of the linear and higher-order terms in  $\theta_{13}$  (and also  $\varepsilon$ ), we compare our results with those generated by the often used sub-dominant approximation which arises from an expansion in the ratio of the mass-squared differences,  $\alpha \equiv \Delta_{12}/\Delta_{32}$ . In this approximation, the leading order oscillation probabilities are given by

$$\begin{aligned} \mathcal{P}_{ee} &= 1 - \sin^2 2\theta_{13} \sin^2(\varphi_{32}) \\ \mathcal{P}_{e\mu} &= \sin^2 \theta_{23} \sin^2 2\theta_{13} \sin^2(\varphi_{32}) \\ \mathcal{P}_{\mu\mu} &= 1 - 4 \cos^2 \theta_{13} \sin^2 \theta_{23} (1 - \cos^2 \theta_{13} \sin^2 \theta_{23}) \\ &\quad \times \sin^2(\varphi_{32}). \end{aligned} \quad (2)$$

Additional correction terms [27, 28, 45] can then be added. The results for the sub-dominant approximation when compared to the results for the full three-neutrino oscillation probabilities will inform us of the size of the correction terms.

We begin by examining the mass-squared difference  $\Delta_{32}$ . We plot  $\Delta\chi^2$  versus  $\Delta_{32}$  using both the sub-dominant approximation, Fig. 1a, and the full three-neutrino calculation, Fig. 1b, with  $\theta_{13}$  and  $\theta_{23}$  as varied parameters. The [black] solid curves are obtained from the Super-K atmospheric data alone. The [red] dash-dot curves employ the K2K, MINOS, and CHOOZ data, omitting the Super-K atmospheric data. These curves are largely determined by the recent MINOS data which constrain the mass-squared difference more so than Super-K, as is well known. The analysis utilizing all of the data sets (atmospheric, K2K, MINOS, and CHOOZ) is depicted by the [blue] dashed curves. Notice that although the Super-K atmospheric data is not as constraining as MINOS, it combines with MINOS to produce a reduced bound, particularly from above. In comparing the approximation, Fig. 1a, with the full calculation, Fig. 1b, we see that the sub-dominant approximation is useful for determining the mass-squared difference  $\Delta_{32}$ . A very careful inspection will reveal that the full three-neutrino analysis produces a slightly larger bound than does the sub-dominant approximation. Our results are  $\Delta_{32} = 0.25_{-0.03}^{+0.02}$  eV<sup>2</sup> at the 90% confidence level. (The errors quoted for our calculations will be for  $\Delta\chi^2 = 6.25$ , the 90% confidence level for a three parameter fit.)

We next present  $\Delta\chi^2$  versus  $\varepsilon = \theta_{23} - \pi/4$  using the sub-dominant approximation, Fig. 2a, and the full three-neutrino calculation, Fig. 2b, with  $\theta_{13}$  and  $\Delta_{32}$  as var-

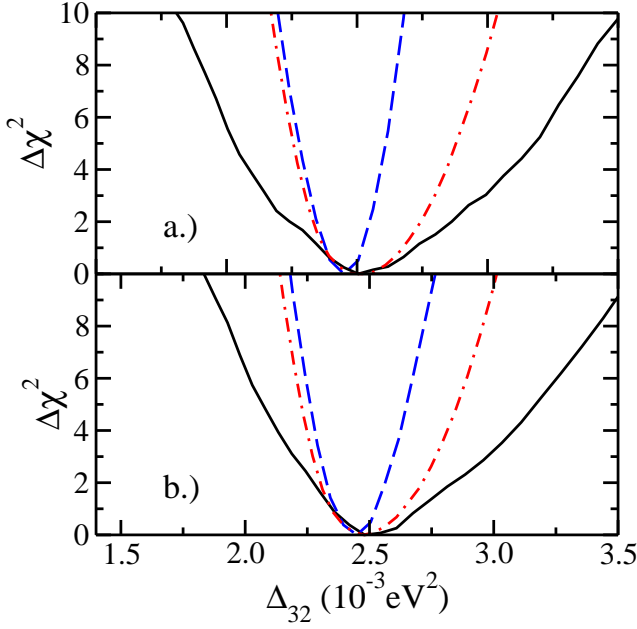


FIG. 1: [color online]  $\Delta\chi^2$  versus mass-squared difference  $\Delta_{32}$  for the a.) sub-dominant approximation and b.) full three-neutrino calculation. The [black] solid curves utilize only atmospheric data; the [red] dot-dash curves utilize K2K, MINOS, and CHOOZ data; the dashed [blue] curves utilize all the data sets: atmospheric, K2K, MINOS, and CHOOZ.

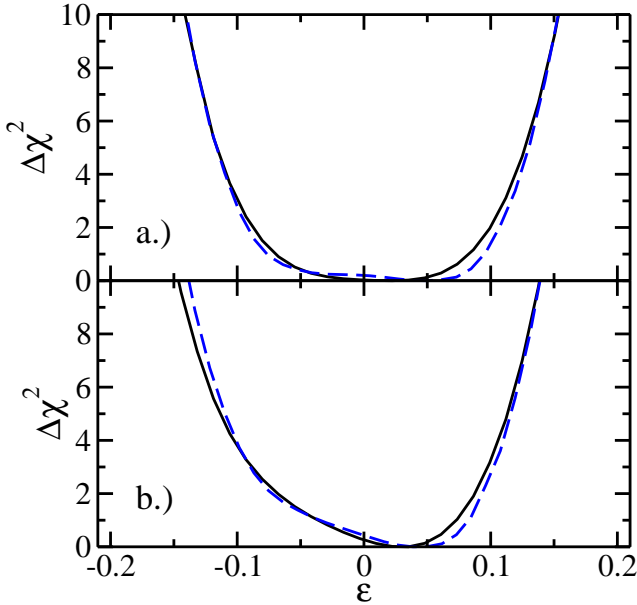


FIG. 2: [color online]  $\Delta\chi^2$  versus  $\epsilon$  for the a.) sub-dominant approximation and b.) full three-neutrino calculation. The [black] solid curve utilizes only atmospheric data; the dashed [blue] curve utilizes all the data sets: atmospheric, K2K, MINOS, and CHOOZ.

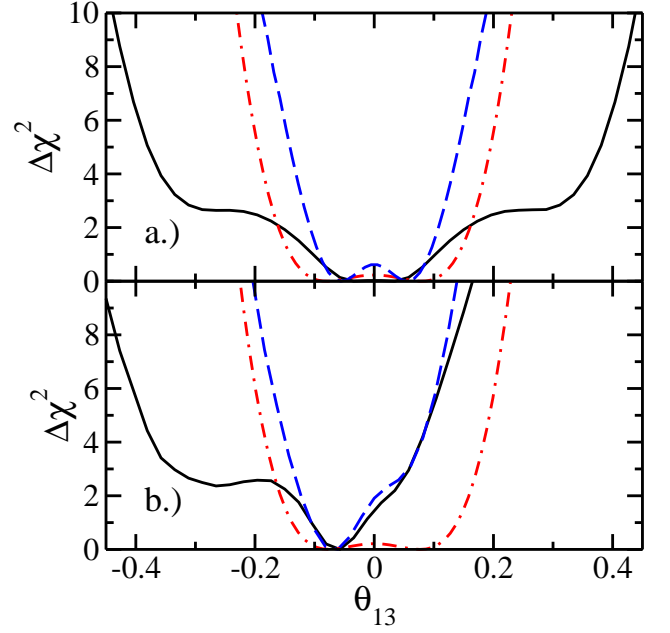


FIG. 3: [color online] The same as Fig. 1 except  $\Delta\chi^2$  versus  $\theta_{13}$  is presented.

ied parameters. We express our result in terms of  $\theta_{23}$ , rather than  $\sin^2 2\theta_{23}$  or  $\sin^2 \theta_{23}$ , because the oscillation probabilities truly are a function of  $\theta_{23}$ . The [black] solid curve again represents the Super-K atmospheric data alone. The [blue] dashed curve represents the results from all data sets: Super-K atmospheric, K2K, MINOS, and CHOOZ. Adding K2K, MINOS, and CHOOZ hardly alters the Super-K result. We do not present the results for K2K, MINOS, and CHOOZ alone because this data does not yield a reasonable constraint on  $\theta_{23}$  when treated as a linear variable with a varied  $\theta_{13}$  included in the analysis. Only in a two neutrino analysis does K2K and MINOS restrict the appropriate variable  $\sin^2 2\theta_{23}$ . Comparing the sub-dominant approximation with the full calculation, we see that the full three-neutrino probabilities produce an allowed region which is much more asymmetric about  $\epsilon = 0$ . In fact, we find a statistically insignificant indication that  $\theta_{23}$  is greater than  $\pi/4$ , maximal mixing. The ability of atmospheric data to determine the octant of  $\theta_{23}$  has also been investigated in [46]. We find the value at 90% CL is  $\epsilon = 0.03^{+0.09}_{-0.15}$ .

In Fig. 3a, we present  $\Delta\chi^2$  versus  $\theta_{13}$  calculated in the sub-dominant approximation and full three-neutrino formulation with  $\theta_{23}$  and  $\Delta_{32}$  as varied parameters. Previously, it has been shown [16] that in the sub-dominant approximation the atmospheric data alone restrict  $\theta_{13}$ . Focusing upon our sub-dominant calculation, Fig. 3a, the [black] solid curve depicts the corresponding result from our analysis. As noted in the Appendix, our analysis quantitatively reproduces the results in Ref. [16]. For  $\Delta\chi^2 < 4.6$ , the 90% confidence level for a two-neutrino analysis, we both find  $\sin^2 \theta_{13} < 0.14$  (or  $|\theta_{13}| < 0.38$ ). This is a very important calibration of our analysis tool.

The effect of  $\theta_{13}$  on atmospheric oscillations is small, and obtaining the same result implies we are reproducing small effects, not just the global features of the analysis. The dash-dot [red] curve in Fig. 3a is the result of analyzing the K2K, MINOS, and CHOOZ data, neglecting the Super-K atmospheric data. This curve is mainly determined by the CHOOZ data. We see that CHOOZ is more constraining on  $\theta_{13}$  than is the Super-K atmospheric data. However, the dashed [blue] curve presents the results utilizing all of the data sets and shows that the Super-K data does somewhat reduce the error on  $\theta_{13}$ ; this is due to the indirect effect arising from Super-K further constraining the mass-squared difference  $\Delta_{23}$ . To obtain the constraints on  $\theta_{13}$  implied by the Super-K atmospheric data, it is important to use the data from Ref. [16] which is more finely binned than earlier Super-K [15] work. Note that the curves in the sub-dominant approximation are symmetric about  $\theta_{13} = 0$  as is manifest from the approximate oscillation formulae, Eq. (2). In Refs. [24, 25, 26], it has been observed that recent data imply a statistically insignificant non-zero value for  $\theta_{13}$ ; our results are likewise consistent.

Turning to the full three-neutrino calculation, Fig. 3b, we find  $\Delta\chi^2$  to be very asymmetric with a strong preference for negative  $\theta_{13}$  when using only Super-K data, the [black] solid curve. The [red] dash-dot curve employs only K2K, MINOS, and CHOOZ data; it is symmetric about the origin so that the asymmetry present when all data is included, the [blue] dashed curve, is due to the Super-K data. What is more, we see the novel result [47] that  $\theta_{13}$  is constrained from above by the Super-K atmospheric data, not by CHOOZ, while it is constrained from below primarily by CHOOZ.

This conclusion is further reinforced by looking at the allowed region for the parameters  $\theta_{13}$  and  $\theta_{23}$  as depicted in Fig. 4. We plot the 90% confidence level of  $\Delta\chi^2 = 4.61$  for a two parameter analysis as we fix the third parameter  $\Delta_{32}$  in calculating these curves. The dash-dot [green] curve depicts the results for Super-K atmospheric data alone in the sub-dominant approximation. We compare this with the dashed [red] curve which also utilizes only the Super-K atmospheric data alone but incorporates the full three-neutrino probabilities. Again, we see the significant change brought about by incorporating the linear, and higher-order, terms in  $\theta_{13}$ . The allowed region grows, favoring negative  $\theta_{13}$ . The dash-dot-dot [blue] curve utilizes all the data in the sub-dominant approximation. It is similar to the dash-dot [green] curve because the mass-squared difference  $\Delta_{32}$  is fixed when calculating the curves; the main effect of the MINOS experiment is to restrict  $\Delta_{32}$ . Finally, the solid [black] curve utilizes all the data and the full three-neutrino oscillation probabilities. Note that the upper bound on  $\theta_{13}$  is similar to that from the dashed [red] curve, i.e. the curve also utilizing the full three-neutrino oscillation probabilities but only the Super-K data. For the lower bound on  $\theta_{13}$ , however, we find similarities to the dash-dot-dot [blue] curve where the restriction on  $\theta_{13}$  originates primarily from the

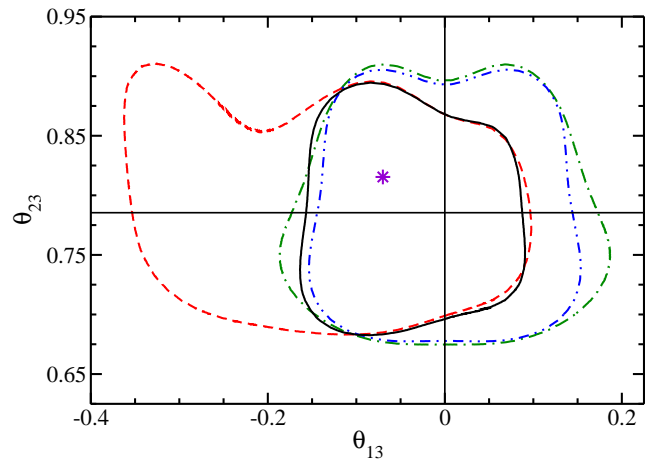


FIG. 4: [color online] The allowed region at 90% CL for the parameters  $\theta_{13}$  and  $\theta_{23}$ . The solid [black] curve uses the full three-neutrino oscillation probabilities and all the data sets: CHOOZ, K2K, MINOS, and Super-K atmospheric. The dash-dot-dot [blue] curve represents the use of the subdominant approximation and all the data sets. The dashed [red] curve depicts the use of the full three-neutrino oscillation probabilities and only the Super-K data. The dash-dot [green] curve depicts the use of the subdominant approximation and the Super-K data alone. The vertical (horizontal) straight line marks  $\theta_{13} = 0$  ( $\theta_{23} = \pi/4$ ). The [violet] star indicates the location of the minimum for the analysis that includes all the data sets and the use of the full three-neutrino oscillation probabilities.

CHOOZ experiment. Thus we again see that the upper bound on  $\theta_{13}$  no longer arises from the CHOOZ experiment but is determined by the Super-K atmospheric experiment, while the lower bound continues to come from the CHOOZ experiment. Our final result for this mixing angle is  $\theta_{13} = -0.07^{+0.18}_{-0.11}$ .

The principle effect of utilizing the full three neutrino oscillation probabilities is the alteration of the shape of the allowed region for  $\theta_{13}$ , particularly the introduction of the asymmetry about zero. The absolute minimum for  $\chi^2$  is lowered by only 1.3 [47]. This is because the minima are very close to  $\theta_{13} = 0$  where the linear and higher order terms contribute little.

### III. DISCUSSION

The most striking differences between the sub-dominant approximation and the full three-neutrino probabilities were seen in the determination of the mixing angle  $\theta_{13}$ , Fig. 3. Additionally, the deviation of  $\theta_{23}$  from maximal mixing also produced noticeable features, though less striking, Fig. 2. Clearly, the two features are non-trivially linked as demonstrated in the allowed regions depicted in Fig. 4. In fact, we see from Fig. 3 that the Super-K data is the source of the asymmetry about  $\theta_{13} = 0$  in the full three-neutrino model. To flesh out

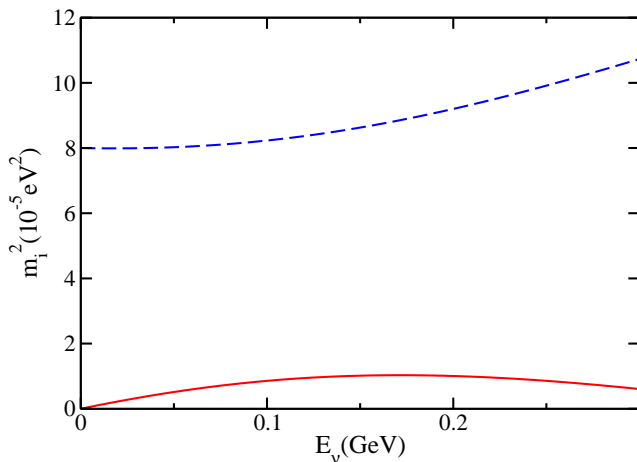


FIG. 5: [color online] The two lowest eigenvalues of the effective mass matrix in a constant density mantle as a function of neutrino energy  $E_\nu$ . The [red] solid curve is  $(m_1)^2(E_\nu)$ , and the [blue] dashed curve is  $(m_2)^2(E_\nu)$ .

which subset of the Super-K data results in these asymmetries, we examine the various contributions of the data to  $\chi^2$  for a fixed positive and negative value of the mixing angle  $\theta_{13}$  taken to be  $\pm 0.15$ . The total difference in  $\Delta\chi^2$  for  $\theta_{13} = +0.15$  and  $\theta_{13} = -0.15$  is  $\sim 7.0$ . Focusing on the fully contained events, we find that two thirds of this change in  $\Delta\chi^2$  between the positive and negative values of the mixing angle comes from the sub-GeV electron-like events. Half of the total change in  $\Delta\chi^2$  (3.5) arises from a single angular bin within this subset of data, namely the bin for  $e$ -like events in which the detected charged lepton has zenith angle  $\vartheta$  satisfying  $-0.8 < \cos \vartheta < -0.6$  and momentum less than 250 MeV. The detected leptons in this bin are produced by neutrinos which travel along a very long baseline upward through the earth. Such neutrinos fall into the region of  $L/E$  where we have previously shown effects linear in  $\theta_{13}$  to be significant in the oscillation probabilities  $\mathcal{P}_{e\mu}$  and  $\mathcal{P}_{\mu\mu}$  [34, 35, 36]; such effects occur in a region where the sub-dominant approximation is the leading term in an expansion which is not convergent. Terms linear in  $\theta_{13}$  can be even more significant [48] should an atmospheric oscillation experiment be able to take data at energies below 100 MeV. We comment that the angular bin,  $-1.0 < \cos \vartheta < -0.8$ , is also in this  $L/E$  region for the low-energy neutrinos; however, a typical neutrino which produces leptons in this bin passes through the earth's higher density core. We find that the core suppresses the oscillations and thus this angular bin is not as sensitive to the effects linear in  $\theta_{13}$ .

The preference of the data for negative  $\theta_{13}$  can be linked to the excess of  $e$ -like events in the sub-GeV data set [37]. This excess is not present in the  $\mu$ -like data or in the multi-GeV data so that an overall renormalization of the atmospheric flux cannot account for the excess. To understand the role of the data in extracting  $\theta_{13}$  and  $\theta_{23}$ , we examine the relevant oscillation probabilities in the

limit of a constant density mantle and sub-GeV neutrino energies, keeping only terms linear in  $\theta_{13}$  and  $\varepsilon$  and averaging over the  $\Delta_{32}$  oscillations; these approximations have been discussed previously [36, 37]. As detailed in the Appendix, the electron-like events at the Super-K detector are related to the  $\nu_e$  survival probability and the  $\nu_\mu$  conversion probability via  $\mathcal{R}_e = \mathcal{P}_{ee} + r\mathcal{P}_{e\mu}$  where  $r$  is the ratio of the  $\nu_\mu$  to  $\nu_e$  flux at the source. This yields the approximate expression

$$\mathcal{R}_e \approx 1 + r \sin^2 2\theta_{12}^m \left[ \frac{1}{2} - \frac{1}{r} + \cot(2\theta_{12}^m) \theta_{13} - \varepsilon \right] \sin^2 \varphi_{21}^m. \quad (3)$$

Here,  $\theta_{12}^m$  is the effective mixing angle in matter; additionally, the phase  $\varphi_{21}^m$  employs the effective mass-squared difference in matter corresponding to  $\Delta_{21}$ . In this approximation, we can understand how to effect an excess of electron-like events for sub-GeV neutrinos over a long baseline,

$$\frac{1}{2} - \frac{1}{r} + \cot(2\theta_{12}^m) \theta_{13} - \varepsilon > 0. \quad (4)$$

Using the same approximations, we can simply express the MSW resonant energy

$$E_R = \frac{\Delta_{21} \cos 2\theta_{12}}{2V \cos^2 \theta_{13}}, \quad (5)$$

with  $V \approx 1.7 \times 10^{-13}$  eV in the mantle; this yields  $E_R$  on the order of 100 MeV. This resonance is apparent when we plot the eigenvalues of the effective mass-squared matrix in the mantle, Fig. 5; the “resonance” is indicated by the slight bowing in the curves toward each other and is located at the point where the effective mass-squared difference is minimal.

At the resonant energy, one has  $\theta_{12}^m = \pi/4$ ; for neutrino energies above the resonance, the effective mixing angle in matter increases up to  $\pi/2$ . As a consequence, for neutrino energies above 100 MeV in the mantle, the function  $\cot(2\theta_{12}^m)$  is negative; to reiterate, the coefficient of the  $\theta_{13}$  term in the inequality, Eq. (4), is negative. We note that for these low energy atmospheric neutrinos  $r \sim 2$  so that the first two terms of the inequality approximately sum to zero. If  $\theta_{13}$  is restricted to positive values, then the mixing angle  $\theta_{23}$  must lie in the first octant ( $\varepsilon < 0$ ) in order to account for the excess in  $\mathcal{R}_e$ . However, if we allow  $\theta_{13}$  to run the full range of allowed parameter space in a CP conserving theory, then a negative value of this mixing angle can easily accommodate the excess in  $\mathcal{R}_e$ , even permitting  $\theta_{23}$  to lie in the second octant as is the case in our analysis.

To demonstrate the point regarding the effect of terms linear in  $\theta_{13}$ , we plot  $\mathcal{R}_e$  in Fig. 6 for sub-GeV neutrinos in angular bin  $-0.8 < \cos \vartheta < -0.6$ . The solid [black] curve employs our best fit parameters. To show the effect of  $\theta_{13}$ , we also plot the  $e$ -like events for  $\theta_{13} = \pm 0.15$  with  $\Delta_{23}$  and  $\theta_{23}$  unchanged. The dash-dot [red] curve has negative  $\theta_{13}$ , and the dashed [blue] curve has positive

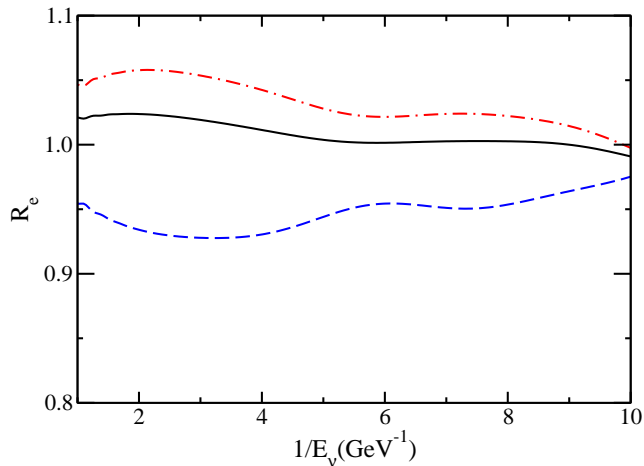


FIG. 6: [color online] The experimentally measured quantity  $R_e$  versus the inverse neutrino energy  $E_\nu^{-1}$  in the sub-GeV region for angular bin  $-0.8 < \cos \vartheta < -0.6$ . The solid [black] curve is the result for the best fit parameters, the dash-dot [red] curve is for  $\theta_{13} = -0.15$  and the dashed [blue] curve is the result for  $\theta_{13} = +0.15$ .

$\theta_{13}$ . It is clear that a negative value of this mixing angle permits an excess of  $e$ -like events for sub-GeV neutrinos.

Returning to Fig. 4, we see how the full three-neutrino oscillation probabilities jointly affect the allowed region for the two mixing angles  $\theta_{23}$  and  $\theta_{13}$ . Using the subdominant approximation, the dash-dot-dot [blue] curve represents the allowed region when all the data is employed. As expected, the region is symmetric about  $\theta_{13} = 0$ , and we note that the actual value of  $\theta_{13}$  has little impact upon the allowed values of  $\theta_{23}$ , save the neighborhood immediately around  $\theta_{13} = 0$ . Inclusion of the higher order terms in the oscillation probability dramatically alters this picture. As discussed above, the data now favor negative  $\theta_{13}$ , with the atmospheric Super-K data shrinking the 90% CL contour, the solid [black] curve, for positive  $\theta_{13}$ . No longer is the contour symmetric about a particular value of  $\theta_{13}$ ; hence, the true value of this mixing angle will impact the allowed region for the  $\theta_{23}$  mixing angle. In particular, the allowed region for  $\theta_{23}$  shrinks as  $\theta_{13}$  approaches positive values. In the future, should a reactor neutrino experiment confirm a nonzero value for  $|\theta_{13}|$ , it will have interesting consequences for the allowed value of  $\theta_{23}$ . With such a measurement, we would perhaps see two true local minima in the  $\Delta\chi^2$  versus  $\theta_{13}$  plot in Fig. 3. The impact upon Fig. 4 would be to separate the jointly allowed regions into two disconnected curves with the limit on  $\theta_{23}$  more tightly constrained for positive values of  $\theta_{13}$ .

#### IV. CONCLUSIONS

As we enter into the era of precision neutrino experiments, small effects, such as those arising from  $\theta_{13}$  or the octant of  $\theta_{23}$ , require a careful treatment in the analysis.

Future reactor experiments [29, 30, 31] are sensitive to  $\theta_{13}^2$  and thus can determine the magnitude of  $\theta_{13}$ , but not its sign. Long-baseline experiments, e.g., [32], will contain small effects that are linear in  $\theta_{13}$ , while an upgraded Super-K will produce additional data in the region where we have found significant effects linear in  $\theta_{13}$ . How these different data interplay with each other in determining  $\theta_{13}$ , including its sign, and the octant of  $\theta_{23}$  will be most interesting.

In Ref. [49], it was shown that the constancy of  $R_e$  imposes an upper bound on  $|\theta_{13}|$  as well as constrains  $\theta_{23}$  to be near maximal mixing. We find that present atmospheric data restrict the value of  $\theta_{13}$  from above, while the limit from below remains as determined by CHOOZ. We find  $\theta_{13} = -0.07_{-0.11}^{+0.18}$ , assuming no CP violation. We have investigated which data points lead to the asymmetry in  $\theta_{13}$  and find that it is the atmospheric data in the very long baseline region previously noted [34, 35, 36] to have significant terms linear in  $\theta_{13}$ . We further found that the Earth's MSW effect plays an important role as it increases the effective value of  $\theta_{12}^m$  in matter such that the atmospheric data provides a strict upper bound on  $\theta_{13}$ . Further, the data producing the preference for a negative  $\theta_{13}$  is data with an excess of  $e$ -like events,  $R_e > 1$ . Allowing  $\theta_{13}$  to be negative supports this excess and permits  $\theta_{23}$  to be in the second octant. The parameters  $\theta_{13}$  and  $\theta_{23}$  are found to be correlated; the statistically insignificant negative value for the minimum of  $\theta_{13}$  relates to the minimum for  $\theta_{23}$  being statistically insignificantly in the second octant, and the error in  $\theta_{23}$  is dependent on the value of  $\theta_{13}$ . Future measurements of  $\theta_{13}$  will impact the allowed value for  $\theta_{23}$ .

For  $\Delta_{32}$  and  $\theta_{23}$  we find  $\Delta_{32} = 0.25_{-0.03}^{+0.02}$  eV<sup>2</sup> and  $\theta_{23} - \pi/4 = 0.03_{-0.15}^{+0.09}$ , where the use of the full three-neutrino oscillation probabilities leads to the asymmetry in the errors. We find that a quantitative analysis requires utilizing the more finely binned atmospheric data of Ref. [16], the use of the full three-neutrino oscillation probabilities, and the inclusion of the full three-neutrino MSW effect.

#### APPENDIX: EXPERIMENTAL SIMULATION

In this appendix, we present the computational tools we use to analyze the Super-K atmospheric, CHOOZ, K2K, and MINOS experiments. The analysis tool for the Super-K atmospheric data is similar to that being used by others [23, 27, 28]; however, it is distinct in that we employ a full three-neutrino oscillation probability rather than an approximate expansion, use a full three-neutrino treatment of the Earth's MSW effect, and include a model of the multi-ring data. The analysis of CHOOZ, K2K, and MINOS data is standard. Additional details can be found in Ref. [50]. Also, in this appendix, we demonstrate the efficacy of our analysis tools by comparing our results with others' when appropriate.

The appendix is organized as follows. We first discuss

the Super-K atmospheric experiment, beginning with the contained events followed by the upgoing muon events. Then we discuss our statistical treatment of this experiment. Finally, we include a similar discussion for the CHOOZ, K2K, and MINOS experiments.

### 1. Super-K contained events

In order to observe atmospheric neutrinos at Super-Kamiokande, the neutrinos must interact with matter in either the detector or the surrounding environ to produced charged particles. The direction and energy of these charged particles can be deduced from the Cherenkov light they emit while traveling through the water-filled detector; from this data, one can infer on average the direction and energy of the initial neutrino. The Super-K experiment classifies the various detections in terms of the production point of the charged lepton, the number of charged particles produced, and their subsequent motion through the detector.

Contained events refer to events in which the charged lepton is produced by the neutrino within the detector. These events are subdivided into fully contained and partially contained events. If an event is fully contained, then the charged lepton(s) produced within the detector do not escape the detector. An event is partially contained if the charged lepton(s) exit the detector. Finally, these two data sets are further separated into single-ring and multi-ring events according to the number of charged particles produced by the neutrino; if only one charged

lepton is observed in the detector, it is termed a single-ring event. We first discuss the fully contained single-ring events and then extend this analysis to the other classes of data. The fully contained single-ring events are statistically the most significant subset of the data and the cleanest to analyze. Preliminary discussions of the analysis technique utilized for the fully contained events can be found in Refs. [51, 52].

The Super-K detector distinguishes between electrons and muons by the fuzziness of the Cherenkov ring generated by the charged lepton; however, the detector cannot differentiate an electron  $e^-$  from a positron  $e^+$  or a  $\mu^-$  from a  $\mu^+$ . Given flavor and charge conservation, the detector can only determine if an event is  $e$ -like, originating from either a  $\nu_e$  or  $\bar{\nu}_e$  interaction, or  $\mu$ -like, originating from either a  $\nu_\mu$  or  $\bar{\nu}_\mu$  interaction. Thus the detector counts charged leptons of flavor  $\alpha$  in energy bin  $m$  and zenith angular bin  $n$  over the run time  $T$

$$N_\alpha^{nm} = \sum_{\nu, \bar{\nu}} \left( \frac{dN_{\alpha \rightarrow \alpha}^{nm}}{dt} + \frac{dN_{\beta \rightarrow \alpha}^{nm}}{dt} \right) T, \quad (\text{A.1})$$

where the quantity  $dN_{\beta \rightarrow \alpha}^{nm}/dt$  represents the rate at which a neutrino, created in the atmosphere with flavor  $\beta$ , will be detected as an  $\alpha$ -like event in the appropriate energy and angular bins within the detector.

This rate depends upon the atmospheric neutrino flux, the neutrino oscillation probability from source to detector, the kinematics of the charged lepton production, and the detector efficiencies. We may write it as

$$\begin{aligned} \frac{dN_{\alpha \rightarrow \beta}^{nm}}{dt} = & N \int_{E_{vis}^{m, min}}^{E_{vis}^{m, max}} dE_{vis} \int d\cos\theta_\nu \int dE_\nu \int d\cos\theta_s \int d\phi_s \\ & \times \varepsilon(E_{vis}) \frac{d^2\Phi_\alpha(E_\nu, \cos\theta_\nu)}{dE_\nu d\cos\theta_\nu} \tilde{\mathcal{P}}_{\alpha\beta}(E_\nu, \cos\theta_\nu) \frac{d^3\sigma_\beta(E_\nu; E_\ell, \cos\theta_s)}{dE_\ell d\cos\theta_s d\phi_s} \\ & \times \Theta(\cos\vartheta^{n, max} - \cos\vartheta) \Theta(\cos\vartheta - \cos\vartheta^{n, min}). \end{aligned} \quad (\text{A.2})$$

We define the variables in Eq. (A.2).  $N$  represents the number of target protons.  $E_{vis}$  is the energy measured by the detector (this quantity is defined differently depending on the data sample);  $E_{vis}^{m, max}$  ( $E_{vis}^{m, min}$ ) is the maximum (minimum) value of  $E_{vis}$  for bin  $m$ . (For single-ring fully contained events,  $E_{vis}$  is simply the energy of the created lepton,  $E_{vis} = E_\ell$ .)  $\vartheta$  is the zenith angle of the detected charged lepton with  $\cos\vartheta = 1$  indicating the vertically downward direction. The relative angle between the incident neutrino and the produced charged lepton are described by the  $\theta_s$  scattering angle and the  $\phi_s$  azimuthal angle. The energy of the incident neutrino is  $E_\nu$  with zenith angle  $\theta_\nu$ . The azimuthally averaged atmospheric neutrino flux for a neu-

trino of flavor  $\alpha$  is  $d^2\Phi_\alpha(E_\nu, \cos\theta_\nu)/dE_\nu d\cos\theta_\nu$  which we take from Ref. [53].  $\varepsilon(E_{vis})$  corresponds to the detection efficiency.  $d^3\sigma_\beta(E_\nu; E_\ell, \cos\theta_s)/dE_\ell d\cos\theta_s d\phi_s$  is the differential cross section for a neutrino of energy  $E_\nu$  and flavor  $\beta$  to produce a charged lepton of flavor  $\beta$  with energy  $E_\ell$  through a scattering angle  $\theta_s$ . Although the differential cross section which occurs in Eq. A.2 does not depend on the azimuthal angle  $\phi_s$ , the geometry that determines in which angular bin an event lies does depend on  $\phi_s$ . This is because the zenith angle  $\vartheta$  of the charged lepton is given in terms of the neutrino zenith angle  $\theta_\nu$  and the scattering angles  $\theta_s$  and  $\phi_s$  by

$$\cos\vartheta = \cos\theta_s \cos\theta_\nu - \sin\theta_s \sin\theta_\nu \cos\phi_s. \quad (\text{A.3})$$

The energy range for atmospheric neutrinos as measured at Super-K requires the use of several cross sections. At low energies, below 1 GeV, the dominant process is charged-current quasi-elastic scattering from the proton and the nucleons in the oxygen nucleus in  $\text{H}_2\text{O}$ , e.g.,  $\bar{\nu}_e + p^+ \rightarrow e^+ + n$  and  $\nu_e + n \rightarrow e^- + p^+$ . At intermediate energies, peaking around 1.5 GeV, the dominant process is single-pion resonance production, i.e.  $\nu_\alpha + N \rightarrow \ell_\alpha + N^*$  followed by  $N^* \rightarrow N' + \pi$ . At higher energies, starting at 1 GeV and dominating above 10 GeV, deeply inelastic scattering occurs,  $\nu_\alpha + N \rightarrow \ell_\alpha + X$ . We utilize the same set of cross sections as was used in Ref. [15]. The Heaviside functions are inserted into Eq. (A.2) in order to restrict the values of  $\theta_\nu$ ,  $\theta_s$ , and  $\phi_s$  to values which produce a value for  $\vartheta$  that lies within bin  $n$ .

The incident neutrino's zenith angle  $\theta_\nu$  does not uniquely determine the path length  $L$ , as neutrinos are produced at a variety of vertical heights  $h$  in the atmosphere. We thus introduce the oscillation probability  $\tilde{\mathcal{P}}_{\alpha\beta}(E_\nu, \cos\theta_\nu)$  averaged over this production height in the atmosphere

$$\tilde{\mathcal{P}}_{\alpha\beta}(E_\nu, \cos\theta_\nu) = \int_0^\infty dh P_\alpha(h, E_\nu) \mathcal{P}_{\alpha\beta}(L(h, \cos\theta_\nu)/E_\nu), \quad (\text{A.4})$$

where  $L$  is related to  $h$  and  $\cos\theta_\nu$  by

$$L = \sqrt{R^2 \cos^2 \theta_\nu + h(2R + h)} - R \cos \theta_\nu, \quad (\text{A.5})$$

with  $R$  the radius of the Earth.  $P_\alpha(h, E_\nu)$  is the normalized probability for a neutrino of flavor  $\alpha$  to be created at a height  $h$ , a quantity we take from Ref. [54].

The neutrino oscillation probability in vacuum  $\mathcal{P}_{\alpha\beta}(L/E_\nu)$  is given in Eq. (1); however, the coherent forward scattering of neutrinos on matter alters the probability for those neutrinos which pass through the Earth [41, 42]. Neutral current interactions between the neutrinos and matter are not flavor dependent leaving the oscillation probabilities unaffected; however, charged current interactions will introduce into the Hamiltonian a flavor dependent potential. In the flavor basis, we may write [55] the neutrino evolution equation as

$$i\partial_t \nu_f = \left[ \frac{1}{2E_\nu} U \mathcal{M} U^\dagger + \mathcal{V} \right] \nu_f \quad (\text{A.6})$$

where  $\mathcal{M} = \text{diag}(0, \Delta_{21}, \Delta_{31})$  and the operator  $\mathcal{V}$  operates on only the electron flavor with a magnitude  $\mathcal{V} = \sqrt{2} G_F N_e(x)$  in which  $N_e(x)$  is the electron number density of the matter. We note that for anti-neutrinos, this potential has the opposite algebraic sign. In matter of constant density, one may diagonalize the Hamiltonian to determine the effective mass-squared differences in a new propagation basis; this basis is related to the flavor states by a modified effective mixing matrix in the matter. The density of the earth may be approximated as piecewise constant [43] so that neutrinos which travel through the earth may traverse regions of varying density. For certain energies and mixing angles, neutrinos can undergo parametric resonances when passing through regions of different densities [44]. For a piecewise constant density profile, we may use the methods of Refs. [39, 40] to exactly determine the neutrino oscillation probability. This method is computationally efficient as it merely involves finding the local effective mass-squared differences and mixing angles, and its exactness accurately accounts for effects which depend on small parameters or effects due to parametric resonances.

The full calculation represented by Eq. (A.2) is a numerically intensive five-dimensional integration. We desire an analysis tool which is both numerically accurate and sufficiently computationally efficient that we can scan a large swath of parameter space in a reasonable amount of time. To effect this, we make approximations in Eq. (A.2) regarding the scattering angle and efficiency terms. First, we fix the scattering angle  $\theta_s$  to its average value  $\bar{\theta}_s$  as a function of  $E_{vis} = E_\ell$  for each energy and angular bin as calculated by the Monte Carlo simulations in Ref. [56]. This eliminates the integral over  $\cos\theta_s$ . We are justified in doing so because, if this integral is done last, the integrand is quite smooth and nearly linear over each bin, particularly for the finer binning of the most recent data. Thus, we expect this approximation to be quantitatively accurate, and this is what we have found. With this approximation, Eq. (A.2) becomes

$$\begin{aligned} \frac{dN_{\alpha\rightarrow\beta}^{nm}}{dt} = & N \int_0^\infty dE_\nu \int_{E_{vis}^{m,min}}^{E_{vis}^{m,max}} dE_{vis} \int d\cos\theta_\nu \int d\phi_s \\ & \times \varepsilon(E_{vis}) \frac{d^2 \Phi_\alpha(E_\nu, \cos\theta_\nu)}{dE_\nu d\cos\theta_\nu} \tilde{\mathcal{P}}_{\alpha\beta}(E_\nu, \cos\theta_\nu) \frac{d^2 \sigma_\beta(E_\nu; E_\ell, \cos\bar{\theta}_s(E_{vis}))}{dE_\ell d\phi_s} \\ & \times \Theta(\cos\vartheta^{n,max} - \cos\vartheta) \Theta(\cos\vartheta - \cos\vartheta^{n,min}), \end{aligned} \quad (\text{A.7})$$

where the differential cross section and the angle  $\vartheta$  have

been evaluated at  $\cos(\theta_s) = \cos(\bar{\theta}_s)$ .

Finally, we must determine the detector efficiency  $\varepsilon(E_{vis})$ , which has not been furnished by the experimentalists. We can, however, extract it from information

---


$$\frac{dN_{\alpha}^m}{dt} = \bar{\varepsilon}(m) N \int_0^{\infty} dE_{\nu} \int_{E_{vis}^{m,min}}^{E_{vis}^{m,max}} dE_{vis} \int d\cos\theta_{\nu} \int d\phi_s \frac{d\Phi_{\alpha}(E_{\nu}, \cos\theta_{\nu})}{dE_{\nu} d\cos\theta_{\nu}} \frac{d^3\sigma_{\beta}(E_{\nu}; E_{\ell}, \cos\bar{\theta}_s(E_{vis}))}{dE_{\ell} d\cos\theta_s d\phi_s} \quad (\text{A.8})$$

where we have assumed that the efficiency is primarily dependent on the lepton energy,  $\varepsilon(E_{vis})$ . Further taking it as a constant  $\bar{\varepsilon}(m)$  over each energy bin  $m$ , we pull it out of the integral. The Monte Carlo calculation of  $dN_{\alpha}^m/dt$  appears in Ref. [57]. Performing the integrals on the right hand side of Eq. (A.8), we can use the Monte Carlo result to determine the average efficiency  $\bar{\varepsilon}(m)$  for each energy bin. This average is then used in Eq. (A.7).

To conclude the discussion of the single-ring fully contained analysis, we note that there are ten angular bins of equal size in  $\cos\vartheta$ , going from +1 (downward) to -1 (upward); ten energy bins for  $e$ -like events; and 8 energy bins for  $\mu$ -like events. In total, this subset of the data consists of 180 data points.

Within the fully contained data set, we also have multi-ring events. This data correspond to neutrinos which interact inside the detector to produce more than one detected particle in the final state. We can calculate the multi-ring event rate in a manner similar to the single-ring event rate provided we modify the visible energy and neutrino event direction. In a multi-ring event, the visible energy depends on the number of particles in the final state, their momenta, and their scattering angles. There is not a simple and reliable way of determining  $E_{vis}$ ; as such, we must make some approximations. We use the results of Monte Carlo simulations in Ref. [56] to estimate the average value of  $E_{\nu}/E_{vis}$  for each energy bin. To determine the angular distribution of these events, we assign a single scattering angle to the final state particles. To make a simple estimate of the average multi-ring scattering angle for each energy bin  $m$ ,  $\bar{\theta}_{s,multi}(m)$ , we fit our no-oscillation event rate to the analogous no-oscillation Monte Carlo calculation from Ref. [57]. Our analysis then uses Eqs. (A.1,A.2,A.3) to calculate the general event rate.

The next data set consists of the partially-contained events. In these, the charged lepton is created within the detector but has sufficient energy to escape the inner detector and be detected by the outer detector (OD). If the energy deposited in the OD appears to be less than

provided. For no oscillations, Eq. (A.2) becomes, utilizing our assumptions,

---

that needed for a muon to traverse the OD, the event is classified as an OD stopped event; those depositing more energy are termed OD through-going. We alter the definition of the visible energy

$$E_{vis} = E_{inner} + E_{dead} + E_{anti}, \quad (\text{A.9})$$

with  $E_{inner}$  the total energy of the charged particle observed in the inner detector,  $E_{dead}$  the energy deposited in the region between the inner detector and the outer detector, and  $E_{anti}$  the energy observed in the outer detector. The charged lepton energy is then a function of this visible energy; we set  $E_{\ell}(E_{vis})$  to its average value as taken from the Monte Carlo calculations from Ref. [56]. The efficiencies are similarly taken for each data bin from the same Monte Carlo no-oscillation calculations as described above. For these single-ring partially contained events, the same ten angular bins are used, and there are four energy bins each for both the OD stopped and through-going events, giving a total of 80 data points.

## 2. Upgoing muons

A second major subset of the atmospheric data arises from detecting muons created by atmospheric neutrinos and anti-neutrinos interacting with the rock surrounding the detector. These muons can then either stop in the detector, called “stopping muons”, or pass through the detector, called “through-going muons”. Typically the stopping muons have an  $\mathcal{O}(10 \text{ GeV})$  energy while the through-going muons have an  $\mathcal{O}(100 \text{ GeV})$  energy. Although statistically not as significant as the contained events, these data provide important information in this higher energy range.

Our analysis of these events exactly follows that given in Refs. [58, 59]. We do not include the effects of the muon energy fluctuations as has recently been done in Ref. [27]. The detection rate for stopping muons,  $S$ , and through-going muons,  $T$ , is given by

$$\begin{aligned} \frac{dN_{\mu,S,T}^n}{dt} &= N_A \int_0^\infty dE_\nu \int_{\theta^{n,min}}^{\theta^{n,max}} d\cos\theta_\nu \int_0^{E_\nu} dE_\mu \\ &\times \frac{d^2\Phi_\alpha(E_\nu, \cos\theta_\nu)}{dE_\nu d\cos\theta_\nu} \tilde{\mathcal{P}}_{\alpha\mu}(E_\nu, \cos\theta_\nu) \frac{d\sigma_\mu(E_\nu; E_\mu)}{dE_\mu} \mathcal{R}(E_\mu, E_{th}) A_{S,T}(E_{th}, \cos\theta_\nu). \end{aligned} \quad (\text{A.10})$$

We have assumed, appropriate for these high energies, that the scattering is forward. This allows us to replace the charged lepton angle  $\vartheta$  with the neutrino angle  $\theta_\nu$ ; we may also perform the integration over the scattering angles  $\theta_s$  and  $\phi_s$  in the cross section.  $N_A$  is Avogadro's number. The function  $\mathcal{R}(E_\mu, E_{th})$  is the average distance that a muon of energy  $E_\mu$  will travel until its energy reaches the value  $E_{th}$ , the amount of energy needed to traverse the detector; this quantity is expressed in the natural units for range, distance times the Earth's density.  $A_T(E_{th}, \cos\theta_\nu)$  is the area projected onto a plane perpendicular to the muon direction such that a muon of energy  $E_{th}$  or greater can pass through this part of the detector. The details for calculating  $A_T(E_{th}, \cos\theta_\nu)$  can be found in Ref. [60]. For the stopping muons,  $A_S(E_{th}, \cos\theta_\nu) = A(\ell_{min}, \cos\theta_\nu) - A_T(E_{th}, \cos\theta_\nu)$ , where  $A(\ell_{min}, \cos\theta_\nu)$  is the projected area of the detector with a path length greater than  $\ell_{min}$  taken to be 7 m by the experimentalists. Note that there is only muon data as electrons/positrons produced in the rock are unable to travel to the detector. The data covers the angular region from  $\cos\theta_\nu = 0$  to  $\cos\theta_\nu = -1$ , directions where muon production from the rock exceeds the cosmic ray background. Since the neutrinos can originate as either electron or muon neutrinos, we sum over the two neutrino flavors  $\alpha$  as in Eq. (A.10). The upgoing muon data is binned in ten angular bins and not binned in energy, resulting in a total of 20 data points.

Analysis of these events is not as computationally intensive as the calculation of the contained events because the forward scattering allows the integration over the scattering angles and the muon energy  $E_\mu$  to be performed outside the fitting program. The parameters being fit are contained in  $\mathcal{P}_{\alpha\mu}(E_\nu, \cos\theta_\nu)$  which is independent of the muon energy and scattering angle. We have found it efficient to change the integration over these variables to the Feynman scaling variables  $x$  and  $y$ , as is natural for the deeply inelastic region.

### 3. Super-K Statistical Analysis

We use the most recent experimental data from Ref. [16] which includes 180 data points for fully contained single-ring events, 90 for fully contained multi-ring events, 80 for partially-contained events, 10 for upward through-going muons, and 10 for upward stopping muons; in all, this constitutes 370 data points. In order to determine the neutrino oscillation parameters, we con-

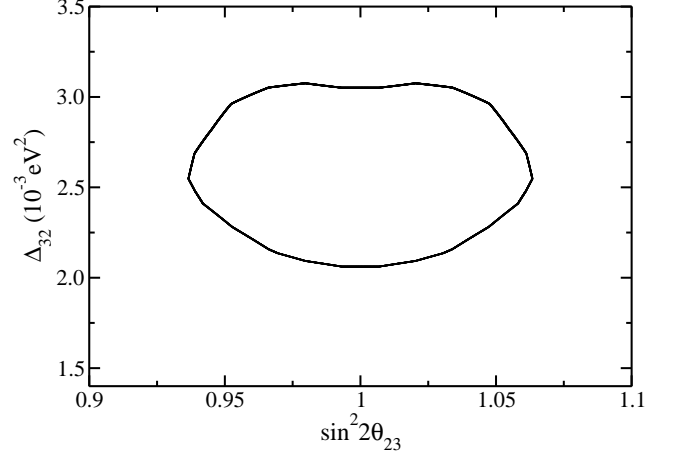


FIG. 7: Allowed region at 90% confidence level for  $\Delta_{32}$  and  $\sin^2 2\theta_{23}$  in the subdominant approximation using only Super-K atmospheric data.

struct a  $\chi^2$  based upon a Poisson distribution, following the same procedure used in Ref. [16]. We incorporate systematic errors by utilizing the “pull” approach as described in Ref. [?], which allows one to incorporate systematic errors in the analysis without adding adjustable parameters. The approach is based upon allowing linear corrections to the theoretical predictions for each systematic error. Our  $\chi^2$  function is

$$\begin{aligned} \chi^2 &= \sum_{n=1}^{370} \left[ 2\{\bar{N}_{the}(n) - N_{obs}(n)\} \right. \\ &\quad \left. + 2N_{obs}(n) \ln \left( \frac{N_{obs}(n)}{\bar{N}_{the}(n)} \right) \right] + \sum_{i=1}^{43} \left( \frac{\xi_i}{\sigma_i} \right)^2. \end{aligned} \quad (\text{A.11})$$

$N_{obs}(n)$  is the number of observed events in the bin  $n$ ;  $N_{the}(n)$  is the theoretical prediction of the number of events in that bin;  $\xi_i$  is the systematic error pull for the systematic error  $i$ ; and  $\sigma_i$  is the one-sigma value for the systematic error  $i$ .  $\bar{N}_{the}(n)$  represents a modified prediction of the expected number of events due to the inclusion of systematic errors; the systematic errors adjust this quantity through an assumed linear dependence on the pulls  $\xi_i$ . Here we use 45 systematic errors arising from different inputs into the data analysis as described in Tables VII–X taken from Ref. [15]. For these 45 errors, all of them contributed to the  $\chi^2$  except the overall

flux normalization and the normalization for the multi-GeV multi-ring sample, which are floated freely. During each fit, these forty-five  $\xi_i$  are varied to minimize  $\chi^2$  for a given set of oscillation parameters. The minimization of  $\chi^2$  with respect to  $\xi_i$  ( $\frac{\partial \chi^2}{\partial \xi_j} = 0$ ) is equivalent in the pull method to numerically solving for  $\xi_i$  in the 45 coupled equations of the form

$$\frac{\partial \chi^2}{\partial \xi_j} = \sum_{n=1}^{370} f_j^n \left( N_{th}(n) - \frac{N_{obs}(n)}{1 + \sum_{i=1}^{45} f_i^n \cdot \xi_i} \right) + \sum_{i=1}^{43} \frac{\xi_i}{\sigma_i^2} \delta_{ij} = 0, \quad (\text{A.12})$$

where  $f_i^n$  is the  $i$ th systematic error for bin  $n$ . These equations are linearized and solved as a set of coupled linear equations.

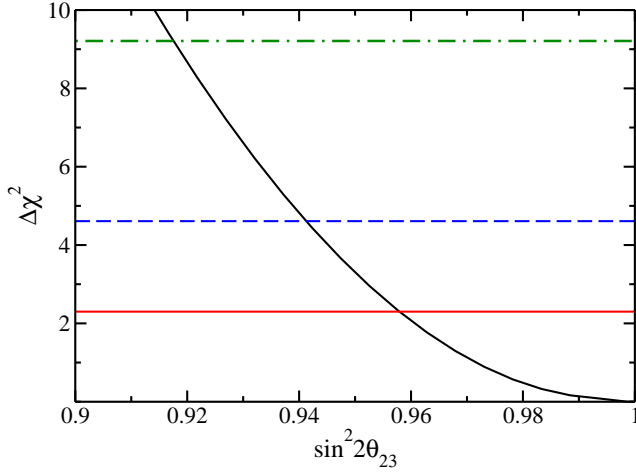


FIG. 8: [color online]  $\Delta\chi^2$  versus  $\sin^2 2\theta_{23}$  for our analysis of the recent Super-K atmospheric data in the sub-dominant approximation. The horizontal lines take the values: [red] solid,  $\Delta\chi^2 = 2.30$ ; [blue] dashed,  $\Delta\chi^2 = 4.61$ ; and [green] dot-dashed,  $\Delta\chi^2 = 9.21$ , the 68%, 90%, and 99% confidence levels for a two parameter fit. Both  $\Delta_{32}$  and  $\theta_{13}$  are varied in obtaining this curve.

We compare our analysis with that performed by the experimentalists in Ref. [16]. To do this, we utilize the sub-dominant approximation in Eq. (2) and minimize the above  $\chi^2$ . Our best fit oscillation parameters are  $(\Delta_{32}, \sin^2 \theta_{23}, \theta_{13}) = (2.5 \times 10^{-3} \text{ eV}^2, 0.51, 0.01)$  with an overall  $\chi^2$  of 416 for the 370 data points. In Fig. 1.a, the [black] solid curve represents  $\Delta\chi^2$  versus  $\Delta_{32}$  for the sub-dominant approximation, using only atmospheric data. In Fig. 7, we present the allowed region for  $\Delta_{32}$  and  $\sin^2 2\theta_{23}$  corresponding to  $\Delta\chi^2 = 4.61$ , the 90% confidence level for a two parameter fit. We also present  $\Delta\chi^2$  versus  $\sin^2 \theta_{23}$  in Fig. 8.

At the 90% confidence level for a two parameter fit, we find the allowed parameter values  $2.1 \times 10^{-3} \text{ eV}^2 < \Delta_{32} < 3.1 \times 10^{-3} \text{ eV}^2$  and  $0.938 < \sin^2 2\theta_{23}$ . Additionally, we extract the allowed value for  $\theta_{13}$  from the [black]

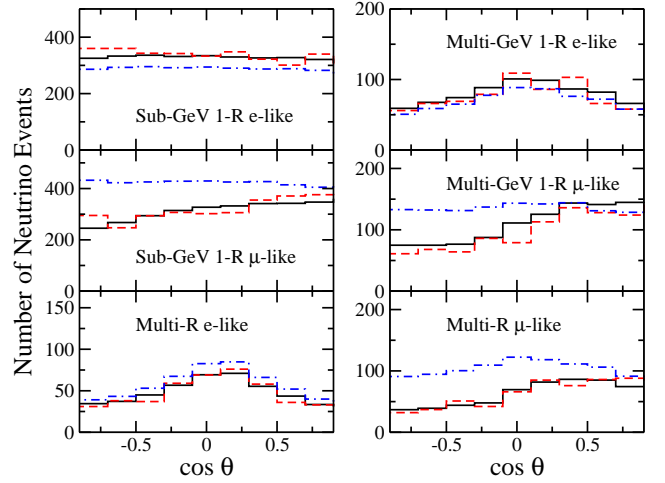


FIG. 9: The top two graphs depict the number of events for the sub-GeV data as a function of the angular bin in  $\cos \theta$ , the middle two graphs are the same except for the multi-GeV data, and the bottom two graphs are for the multi-ring events. The [black] solid curves represent the results from our best fit parameters, the [red] dashed curves represent the data, and the [blue] dot-dashed curves represent the Monte Carlo no-oscillation predictions.

solid curve in Fig. 3a,  $-0.38 < \theta_{13} < 0.38$ . This is exactly the result of Ref. [16], and our other results are in excellent agreement with that analysis. As noted previously, our reproduction of the allowed region for  $\theta_{13}$ , which has a nonzero but small effect on the atmospheric data, is a very strong test of our analysis.

Finally, in Figs. 9 and 10, we compare the predicted number of neutrino events corresponding to our best fit parameters with the experimental data as a function of the zenith angle. We also present the Monte Carlo predictions for the expected number of events in the absence of neutrino oscillations. Each of the different Super-K atmospheric data sets is depicted. The results are a good fit to the data, comparable to that found in Ref. [16].

#### 4. CHOOZ experiment

For the CHOOZ reactor experiment, we follow a standard procedure as described in Ref. [21]. In our analysis, we use experimental data that consists of seven positron energy bins for each of the two reactors, giving a total of 14 bins. We include a  $14 \times 14$  covariance matrix,  $V_{ij}^{-1}$ , to account for the correlation between the energy bins, and we include the systematic error from the overall normalization and energy calibration. We write the expected positron yield for the  $k^{th}$  reactor and the  $j^{th}$  energy spectrum bin as

$$\overline{X}(E_j, L_k, \theta, \Delta_{32}) = \tilde{X}(E_j) \overline{P}(E_j, L_k, \theta, \Delta_{32}), \quad (j = 1, \dots, 7, k = 1, 2), \quad (\text{A.13})$$

where  $\tilde{X}(E_j)$  is the distance-independent positron yield in the absence of neutrino oscillations,  $L_k$  is the reactor-detector distance, and  $\overline{P}(E_j, L_k, \theta, \Delta_{32})$  is the oscillation probability averaged over the energy bin and the detector

$$\chi^2(\theta, \Delta_{32}, \alpha, g) = \sum_{i=1}^{14} \sum_{j=1}^{14} \left( X_i - \alpha \overline{X}(gE_i, L_i, \theta, \Delta_{32}) \right) V_{ij}^{-1} \left( X_j - \alpha \overline{X}(gE_j, L_j, \theta, \Delta_{32}) \right) + \left( \frac{\alpha - 1}{\sigma_\alpha} \right)^2 + \left( \frac{g - 1}{\sigma_g} \right)^2, \quad (\text{A.14})$$

with the absolute normalization constant  $\alpha$  and the energy-scale calibration factor  $g$ .

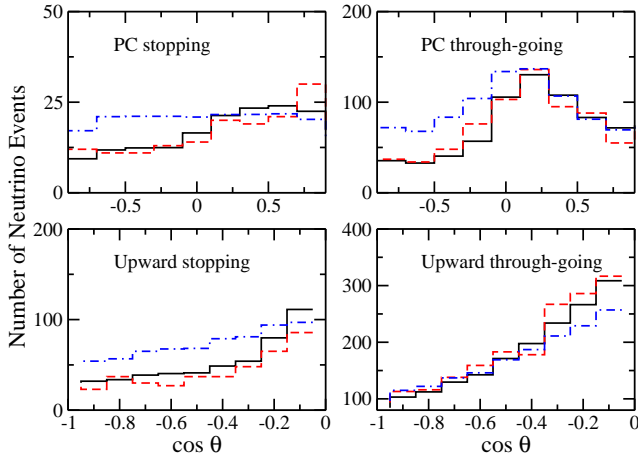


FIG. 10: The same as Fig. 9 except the data sets are now the partially contained stopping events (upper left), the partially contained through-going events (upper right), the upward stopping muon events (lower left), and the upward through-going muon events (lower right).

## 5. K2K experiment

For the K2K experiment [20], we employ the method developed in Ref. [61] to estimate the expected no-oscillation neutrino spectrum,  $S(E_\nu)$ , in the relevant energy range of  $\sim 0.2$  to  $\sim 3.0$  GeV. The expected number of neutrino events for oscillating neutrinos is then

$$N_n^{theo} = \int_{E_{min}(n)}^{E_{max}(n)} S(E_\nu) P_{\mu\mu}(L/E_\nu), \quad (\text{A.15})$$

where  $P_{\mu\mu}(L/E_\nu)$  is the muon neutrino survival probability and  $E_{max}(n)$  ( $E_{min}(n)$ ) are the maximum (minimum) energy values for the energy bin  $n$ . For the statistical analysis, we follow the procedure described in Ref. [62]. We only use the single-ring sub-sample, which consist of

and reactor core sizes. In our fitting routine, we minimize the following  $\chi^2$  function with respect to the neutrino oscillation parameters

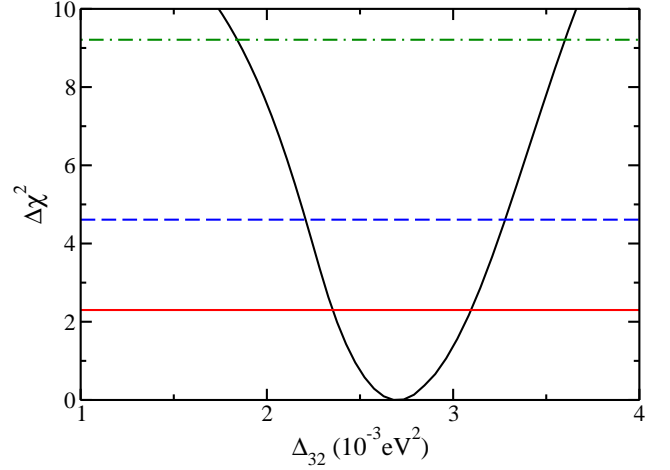


FIG. 11: [color online]  $\Delta\chi^2$  versus  $\Delta_{32}$  for our analysis of the K2K experiment in the sub-dominant approximation. The horizontal lines take the values: [red] solid,  $\Delta\chi^2 = 2.30$ ; [blue] dashed,  $\Delta\chi^2 = 4.61$ ; and [green] dot-dashed,  $\Delta\chi^2 = 9.21$ , the 68%, 90%, and 99% confidence levels for a two parameter fit.

58 neutrino events. The signature for neutrino oscillations from  $\nu_\mu$  to  $\nu_\tau$  in a two neutrino analysis are both a reduction in the total number of observed neutrino events and a distortion in the neutrino energy spectrum. The  $\chi^2$  function is divided into two terms: the observed total number of events detected at the Super-K detector,  $\chi_{norm}^2$ , and the shape of the spectrum included in  $\chi_{shape}^2$ . We use the “pull” method [?] to account for 31 systematic uncertainties by adding a third term  $\chi_{syst}^2$ .

$$\chi_{K2K}^2 = \chi_{norm}^2 + \chi_{shape}^2 + \chi_{syst}^2. \quad (\text{A.16})$$

The best fit oscillation parameters,  $\Delta_{32}$  and  $\theta_{23}$ , are obtained by minimizing  $\chi_{K2K}^2$ .

The systematic parameters included in  $\chi_{syst}^2$  arise from the neutrino energy spectrum at the near detector site, the flux ratio, the neutrino-nucleus cross-section, the efficiency and the energy scale of the Super-K detector, and the overall normalization. The  $k$ th systematic error is represented by the coefficient  $C_n^k$  and modifies the expected number of neutrino events, Eq. (A.15), in a linear

manner according to the “pull” method

$$\begin{aligned}\tilde{N}_n^{\text{theo}} &= N_n^{\text{theo}}(n) + \sum_{k=1}^{31} C_n^k \xi_k, \\ \tilde{N}_{\text{total}}^{\text{theo}} &= \sum_{n=1}^8 \tilde{N}_n^{\text{theo}},\end{aligned}\quad (\text{A.17})$$

with  $\xi_k$  the pull corresponding to systematic error  $k$ .

Due to the low statistics, we employ a Poisson distribution; hence, the expressions for  $\chi_{\text{norm}}^2$  and  $\chi_{\text{shape}}^2$  are given by

$$\begin{aligned}\chi_{\text{norm}}^2 &= 2 \left( \tilde{N}_{\text{total}}^{\text{theo}} - N_{\text{total}}^{\text{data}} - N_{\text{total}}^{\text{data}} \ln \frac{\tilde{N}_{\text{total}}^{\text{theo}}}{N_{\text{total}}^{\text{data}}} \right), \\ \chi_{\text{shape}}^2 &= 2 \sum_{n=1}^8 \left( \tilde{N}_n^{\text{theo}} - N_n^{\text{data}} - N_n^{\text{data}} \ln \frac{\tilde{N}_n^{\text{theo}}}{N_n^{\text{data}}} \right),\end{aligned}\quad (\text{A.18})$$

where  $N_n^{\text{data}}$  is the experimental data provided by the K2K collaboration [20] and the superscript “total” implies a sum over  $n$ . The contribution to  $\chi^2$  from the systematic errors is

$$\chi_{\text{syst}}^2 = \sum_{j,k=1}^{31} \xi_k M_{kj}^{-1} \xi_j, \quad (\text{A.19})$$

where we use an error matrix  $M_{kj}$  constructed from Tables 8.1 and 8.2 provided in Ref. [62].

In Fig. 11, we depict  $\Delta\chi^2$  versus  $\Delta_{32}$  for an analysis that utilizes only the K2K data in the subdominant approximation; also, Fig. 12 shows the 90% CL allowed region in the [red] dashed contour for  $\Delta_{32}$  and  $\sin^2 2\theta_{23}$  in the subdominant approximation. The absolute minimum in our fit is  $(\Delta_{32}, \sin^2 2\theta_{23}) = (2.78 \times 10^{-3} \text{ eV}^2, 0.998)$ . At 90% CL, we find  $2.2 \times 10^{-3} \text{ eV}^2 < \Delta_{32} < 3.2 \times 10^{-3} \text{ eV}^2$ . The total number of observed events 58 is in agreement with the 56 events found from the model. All of these results are consistent with the analysis performed by the experimentalists in Ref. [20].

## 6. MINOS experiment

The MINOS experiment is quite similar to the K2K experiment and thus we apply a similar analysis technique. For the no-oscillation spectrum, we use the Monte Carlo simulation provided by the MINOS collaboration [18]. We normalized this spectrum to measurements made at the near detector. A total of 1065 events were expected in the absence of neutrino oscillations. With the no-oscillation spectrum and Eq. (A.15), we calculate the expected number of neutrino events in the presence of neutrino oscillations. We use the MINOS data [18] corresponding to two years of beam operation in which 884  $\nu_\mu$  neutrino events are observed. The data consists of

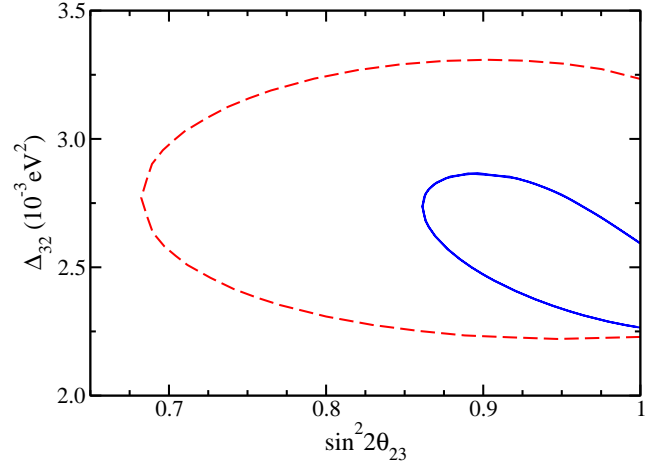


FIG. 12: [color online]  $\Delta_{32}$  vs  $\sin^2 2\theta_{23}$  allowed region for a two parameter fit in the subdominant approximation at the 90% CL for the K2K data, [red] dashed, and the MINOS, [blue] solid, experiments.

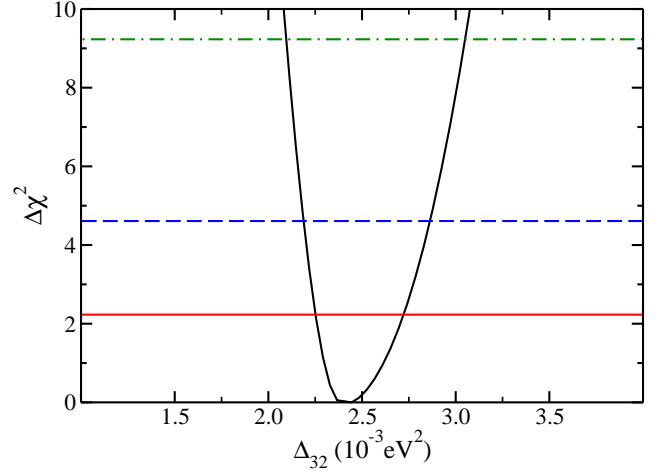


FIG. 13: [color online] The same as Fig. 11 except the data are from MINOS.

15 energy bins along with three systematic errors: the relative normalization between the far and near detectors with a 4% uncertainty; the absolute hadronic energy scale with a 11% uncertainty; and a 50% uncertainty in the neutral-current background rate. For the definition of  $\chi^2$ , we use the Poisson distribution function

$$\begin{aligned}\chi_{\text{MINOS}}^2 &= 2 \sum_{n=1}^{15} \left( \tilde{N}_n^{\text{theo}} - N_n^{\text{data}} - N_n^{\text{data}} \ln \frac{\tilde{N}_n^{\text{theo}}}{N_n^{\text{data}}} \right) \\ &\quad + \sum_{j=1}^3 \left( \frac{\xi_j}{\sigma_j} \right)^2,\end{aligned}\quad (\text{A.20})$$

where the symbols are analogously defined to those in the K2K section.

In Fig. 13 we plot  $\Delta\chi^2$  versus  $\Delta_{32}$  for the K2K data in the subdominant approximation; likewise, in Fig. 12,

we present the allowed region at 90% CL, the [blue] solid curve, for  $\Delta_{32}$  and  $\sin^2 2\theta_{23}$ . The minimum of  $\chi^2$  is located at  $\Delta_{32} = 2.41 \times 10^{-3} \text{ eV}^2$  and  $\sin^2 2\theta_{23} = 0.9990$ . The allowed intervals of these parameters at 90 % CL are  $2.25 \times 10^{-3} \text{ eV}^2 < \Delta_{32} < 2.8 \times 10^{-3} \text{ eV}^2$  and  $0.86 < \sin^2 2\theta_{23}$  for  $\Delta\chi^2 = 4.6$ . All of these results are consistent with the analysis performed by the experimentalists in Ref. [18].

Results which combine CHOOZ, K2K, and MINOS are presented in the main body of this work. This Appendix provides details of the analysis tools we use throughout this work; additional details may be found in Ref. [50].

## APPENDIX: ACKNOWLEDGMENTS

The work of J. E. R. and D. J. E. is supported, in part, by US Department of Energy Grant DE-FG02-96ER40975. The work of J. E. R. is also supported, in part, by CONACyT, Mexico. The work of D. C. L. is supported, in part, by US Department of Energy Grant DE-FG02-96ER40989.

- 
- [1] Y. Fukuda et al. (Kamiokande), Phys. Rev. Lett. **77**, 1683 (1996).
  - [2] M. B. Smy et al. (Super-Kamiokande), Phys. Rev. **D69**, 011104 (2004).
  - [3] B. T. Cleveland et al., Astrophys. J. **496**, 505 (1998).
  - [4] W. Hampel et al. (GALLEX), Phys. Lett. **B447**, 127 (1999).
  - [5] J. N. Abdurashitov et al. (SAGE), J. Exp. Theor. Phys. **95**, 181 (2002).
  - [6] M. Altmann et al. (GNO), Phys. Lett. **B616**, 174 (2005).
  - [7] S. N. Ahmed et al. (SNO), Phys. Rev. Lett. **92**, 181301 (2004).
  - [8] B. Aharmim et al. (SNO), Phys. Rev. **C72**, 055502 (2005).
  - [9] B. Aharmim et al. (SNO), Phys. Rev. **C75**, 045502 (2007).
  - [10] B. Aharmim et al. (SNO), Phys. Rev. Lett. **101**, 111301 (2008).
  - [11] T. Araki et al. (KamLAND), Phys. Rev. Lett. **94**, 081801 (2005).
  - [12] S. Abe et al. (KamLAND), Phys. Rev. Lett. **100**, 221803 (2008).
  - [13] Y. Fukuda et al. (Super-Kamiokande), Phys. Rev. Lett. **81**, 1562 (1998).
  - [14] S. Fukuda et al. (Super-Kamiokande), Phys. Rev. Lett. **85**, 3999 (2000).
  - [15] Y. Ashie et al. (Super-Kamiokande), Phys. Rev. Lett. **93**, 101801 (2004).
  - [16] J. Hosaka et al. (Super-Kamiokande), Phys. Rev. **D74**, 032002 (2006).
  - [17] P. Adamson et al. (MINOS), Phys. Rev. **D77**, 072002 (2008).
  - [18] P. Adamson et al. (MINOS), Phys. Rev. Lett. **101**, 131802 (2008).
  - [19] E. Aliu et al. (K2K), Phys. Rev. Lett. **94**, 081802 (2005).
  - [20] M. H. Ahn et al. (K2K), Phys. Rev. **D74**, 072003 (2006).
  - [21] M. Apollonio et al. (CHOOZ), Phys. Lett. **B466**, 415 (1999).
  - [22] C. Amsler et al. (Particle Data Group), Phys. Lett. **B667**, 1 (2008).
  - [23] T. Schwetz, M. Tortola, and J. W. F. Valle, New J. Phys. **10**, 113011 (2008).
  - [24] G. L. Fogli, E. Lisi, A. Marrone, A. Palazzo, and A. M. Rotunno, Phys. Rev. Lett. **101**, 141801 (2008).
  - [25] A. B. Balantekin and D. Yilmaz, J. Phys. **G35**, 075007 (2008).
  - [26] M. Maltoni and T. Schwetz (2008), arXiv:0812.3161 [hep-ph].
  - [27] M. C. Gonzalez-Garcia and M. Maltoni, Phys. Rept. **460**, 1 (2008).
  - [28] G. L. Fogli, E. Lisi, A. Marrone, and A. Palazzo, Prog. Part. Nucl. Phys. **57**, 742 (2006).
  - [29] X. Guo et al. (Daya Bay) (2007), arXiv:0701029 [hep-ex].
  - [30] F. Ardellier et al. (Double CHOOZ) (2006), arXiv:0606025 [hep-ex].
  - [31] K. K. Joo (RENO), Nucl. Phys. Proc. Suppl. **168**, 125 (2007).
  - [32] Y. Oyama (2005), arXiv:0512041 [hep-ex].
  - [33] M. Raidal et al., Eur. Phys. J. **C57**, 13 (2008).
  - [34] D. C. Latimer and D. J. Ernst, Phys. Rev. **D71**, 017301 (2005).
  - [35] D. C. Latimer and D. J. Ernst, Phys. Rev. **C71**, 062501 (2005).
  - [36] D. C. Latimer and D. J. Ernst, Phys. Rev. **C72**, 045502 (2005).
  - [37] O. L. G. Peres and A. Y. Smirnov, Nucl. Phys. **B680**, 479 (2004).
  - [38] D. C. Latimer, J. Escamilla, and D. J. Ernst, Phys. Rev. **C76**, 055502 (2007).
  - [39] T. Ohlsson and H. Snellman, Phys. Lett. **B474**, 153 (2000), hep-ph/9912295.
  - [40] T. Ohlsson and H. Snellman, J. Math. Phys. **41**, 2768 (2000), hep-ph/9910546.
  - [41] S. P. Mikheev and A. Y. Smirnov, Sov. J. Nucl. Phys. **42**, 913 (1985).
  - [42] L. Wolfenstein, Phys. Rev. **D17**, 2369 (1978).
  - [43] A. M. Dziewonski and D. L. Anderson, Phys. Earth Planet. Inter. **25**, 297 (1981).
  - [44] E. K. Akhmedov, A. Dighe, P. Lipari, and A. Y. Smirnov, Nucl. Phys. **B542**, 3 (1999).
  - [45] E. K. Akhmedov, R. Johansson, M. Lindner, T. Ohlsson, and T. Schwetz, JHEP **04**, 078 (2004).
  - [46] S. Choubey and P. Roy, Phys. Rev. **D73**, 013006 (2006).
  - [47] J. Escamilla, D. C. Latimer, and D. J. Ernst (2008), arXiv:0805.2924 [nucl-th].
  - [48] O. L. G. Peres and A. Y. Smirnov (2009), arXiv:0903.5323 [hep-ph].
  - [49] D. V. Ahluwalia, Mod. Phys. Lett. **A13**, 2249 (1998).
  - [50] J. E. Roa, PhD Thesis, Vanderbilt University, (December 2008).
  - [51] J. Escamilla, D. C. Latimer, and D. J. Ernst, AIP Conf. Proc. **947**, 227 (2007).

- [52] J. Escamilla, D. J. Ernst, and D. C. Latimer, AIP Conf. Proc. **991**, 153 (2008).
- [53] M. Honda, T. Kajita, K. Kasahara, and S. Midorikawa, Phys. Rev. **D70**, 043008 (2004).
- [54] T. K. Gaisser and T. Stanev, Phys. Rev. D **57**, 1977 (1998).
- [55] K. C. Hannabuss and D. C. Latimer, J. Phys. **A33**, 1369 (2000).
- [56] M. D. Messier, PhD Thesis, Boston University (1999).
- [57] M. Ishitsuka, PhD Thesis, University of Tokyo (2004).
- [58] N. Fornengo, M. C. Gonzalez-Garcia, and J. W. F. Valle, JHEP **07**, 006 (2000).
- [59] M. C. Gonzalez-Garcia, M. Maltoni, C. Pena-Garay, and J. W. F. Valle, Phys. Rev. **D63**, 033005 (2001).
- [60] P. Lipari and M. Lusignoli, Phys. Rev. **D58**, 073005 (1998).
- [61] G. L. Fogli, E. Lisi, A. Marrone, D. Montanino, and A. Palazzo, Phys. Rev. **D66**, 053010 (2002).
- [62] M. Hasegawa, PhD Thesis, Kyoto University, (January 2006).